Charge compensation in extremely large magnetoresistance materials LaSb and LaBi revealed by first-principles calculations

Peng-Jie Guo, Huan-Cheng Yang, Bing-Jing Zhang, Kai Liu,* and Zhong-Yi Lu†
Department of Physics, Renmin University of China, Beijing 100872, China
and Beijing Key Laboratory of Opto-electronic Functional Materials & Micro-nano Devices, Renmin University of China, Beijing 100872, China
(Received 25 February 2016; revised manuscript received 28 April 2016; published 21 June 2016)

By the first-principles electronic structure calculations, we have systematically studied the electronic structures of recently discovered extremely large magnetoresistance (XMR) materials LaSb and LaBi. We find that both LaSb and LaBi are semimetals with the electron and hole carriers in balance. The calculated carrier densities on the order of 10^{20} cm^{-3} are in good agreement with the experimental values, implying long mean-free time of carriers at low temperatures and thus high carrier mobilities. With a semiclassical two-band model, the charge compensation and high carrier mobilities naturally explain: (i) the XMR observed in LaSb and LaBi, (ii) the nonsaturating quadratic dependence of XMR on an external magnetic field, and (iii) the resistivity plateau in the turn-on temperature behavior at very low temperatures. The explanation of these features without resorting to the topological effect indicates that they should be the common characteristics of all electron-hole compensated semimetals.

DOI: 10.1103/PhysRevB.93.235142

I. INTRODUCTION

The magnetoresistance (MR) effect, which describes the magnetic-field-induced change in electrical resistance, not only continuously provides exciting physical phenomena since its discovery in 1857 [1], but also brings revolution to human beings' modern lives through its device applications, such as hard drives [2] and magnetic sensors [3]. Until now, many kinds of magnetoresistance effects have been identified. The conventional MR found in simple metals is on the order of a few percent [4,5]. The other well-known MR effects, including the giant magnetoresistance in magnetic multilayers [6,7], the colossal magnetoresistance in perovskite manganites [8], and the tunnel magnetoresistance in magnetic tunnel junctions [9], are more prominent than the conventional MR. Recently, much attention has been paid to the extremely large magnetoresistance (XMR) around 10^4–10^6 percent discovered in a few semimetals: WTe_2 [10], NbP [11], Cd_3As_2 [12], LaSb [13], etc. The most astonishing finding is that the XMR in WTe_2 does not saturate even under a magnetic field as high as 60 T [10].

Several mechanisms have been proposed to explain the XMR found in these semimetals. The quadratic dependence of MR on a perpendicular magnetic field without saturation in WTe_2 can be described by the electron-hole compensation from a semiclassical two-band model [10,14]. The exotic longitudinal linear MR with a magnetic field parallel to the current direction in WTe_2 is explained from a quantum viewpoint by incorporating Landau levels [15]. Previously, the quantum scenario [16] was also applied to the linear MR of nonstoichiometric silver chalcogenides in a perpendicular magnetic field [17]. Besides, the suppression of backscattering channels at zero field and their opening under finite magnetic fields are suggested to play an important role in the magnetoresistance of WTe_2 [18] and the Dirac semimetal Cd_3As_2 [12]. Recently, similar to that found in WTe_2 [10], the nonsaturating XMRs with a quadratic dependence on the magnetic field were observed in two rare-earth monopnictides LaSb [13,19] and LaBi [19–21]. Nevertheless, a consensus has not been achieved on the origin of their nonsaturating XMRs [13,19–21]. To be specific, whether the semiclassical, quantum, or backscattering mechanism applies in this case remains to be verified. Furthermore, LaSb and LaBi are predicted to be three-dimensional topological insulators [22], which adds more concern to these lanthanum monopnictides.

In addition to sophisticated experimental tools, first-principles calculations have also played an important role in interpreting the electronic structures and the nonsaturating XMR of WTe_2 [10,18,23]. As to LaSb and LaBi, the previous calculations by using the augmented-plane-wave method with two different formalisms, i.e., the local density approximation (LDA) and the Slater exchange potential, give distinct band structures for LaSb yet similar ones for LaBi [24]. The calculations based on the Slater exchange potential agree better with the de Haas–van Alphen effect measurements [24–26]. It has been known that for the exchange-correlation functionals, according to Perdew *et al.*, there are several rungs in "Jacob's ladder" of density functional approximations [27], which describe the materials' properties in different levels with increasing computing load. The LDA in the first rung with electron densities and the generalized gradient approximation (GGA) in the second rung with both electron densities and their gradients perform very well in studying the properties of a variety of systems [28]. Nevertheless, due to the derivative discontinuity of the exchange-correlation energy [29,30], the LDA and GGA usually underestimate the band gaps of semiconductors. The meta-GGA in the third rung includes Laplacians of electron density and the kinetic-energy densities beyond the GGA. It gives more accurate band gaps for semiconductors, similar to the ones given by the hybrid functional or GW methods but with much less computational demand [31,32]. The recently discovered XMR materials, including LaSb [13,19] and LaBi [19–21], are semimetals with low carrier densities. Since their electronic structures

*kliu@ruc.edu.cn
†zlu@ruc.edu.cn

 ©2016 American Physical Society

with carrier densities are between those of metals and semiconductors, whether the first-principles calculations at the GGA and the meta-GGA levels would give consistent results on the XMR mechanism of semimetals LaSb and LaBi waits to be unraveled.

In this paper, we report systematic studies on the electronic structures of LaSb and LaBi by using the first-principles electronic structure calculations. Two levels of exchange-correlation functionals, the GGA and the meta-GGA, respectively, are adopted. Although they give somewhat different band structures and distinct band overlaps at certain k points in the Brillouin zone (BZ), the calculated Fermi surfaces and the derived ratio of electron-type and hole-type carrier densities point to the same conclusion that the extremely large MR of LaSb and LaBi originates from the electron-hole compensation.

II. COMPUTATIONAL DETAILS

To study the electronic structures of LaSb and LaBi from first principles, we carried out calculations with the projector augmented-wave method [33,34] as implemented in the VASP package [35–37]. For the exchange-correlation functional, we adopted two different levels in Jacob's ladder [27]: the GGA and the meta-GGA. In the GGA level, the Perdew-Burke-Ernzerhof (PBE) formulas [38] were used, whereas in the meta-GGA level, the modified Becke-Johnson (MBJ) exchange potential [31,32] in combination with the GGA correlation was employed.

The kinetic-energy cutoff of the plane-wave basis was set to be 300 eV. For the Brillouin-zone sampling, a $20 \times 20 \times 20$ dense k-point mesh was utilized for the primitive cell, which contains one formula unit (f.u.), of these rock-salt structural crystals. The Gaussian smearing with a width of 0.05 eV was adopted around the Fermi surface. Both cell parameters and internal atomic positions were fully relaxed until all forces on the atoms were smaller than 0.01 eV/Å. The calculated lattice constants of 6.56 Å for LaSb and 6.67 Å for LaBi with the PBE functional are in good accord with the experimental values of 6.49 and 6.58 Å [20,39], respectively. After the equilibrium structures were obtained, the electronic structures were calculated by including the spin-orbit-coupling (SOC) effect. To accurately describe the subtle electronic structures of LaSb and LaBi around the Fermi level, we have tested the $16 \times 16 \times 16$, $20 \times 20 \times 20$, and $24 \times 24 \times 24$ k-point meshes. We found that the $20 \times 20 \times 20$ k-point mesh renders converged band structures for the calculations based on the MBJ potential. The maximally localized Wannier functions' [40,41] method was then used to calculate the Fermi surfaces, and the carrier concentrations were computed based on the information of Fermi-surface volumes.

III. RESULTS AND ANALYSIS

A. LaSb

Figure 1 shows the band structure along high-symmetry directions of the BZ and the Fermi surface of LaSb calculated with the PBE functional and including the SOC effect. Here we only focus on the bands around the Fermi level. We have checked that, except for those bands displayed in Fig. 1(a),

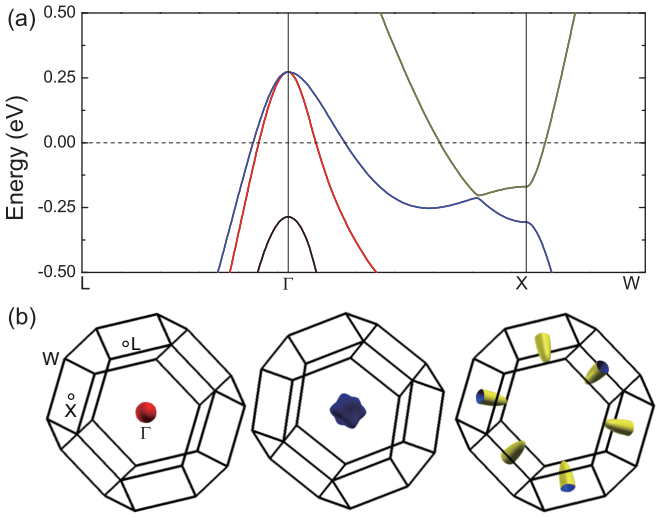

FIG. 1. (a) Band structure along high-symmetry directions of the Brillouin zone and (b) Fermi surface of LaSb calculated with the PBE functional and including the SOC effect.

there is no band crossing the Fermi level along other high-symmetry directions in the BZ, demonstrating the semimetallic behavior of LaSb. For the nonmagnetic rock-salt structural LaSb, due to its space inversion symmetry and time inversion symmetry, the electronic bands are exactly doubly degenerate at zero magnetic field. Since two branches of every band coincide with each other completely, we can only discern one branch of each band from the figure. As can be seen, there are two doubly degenerate bands across the Fermi level around the Γ point and one doubly degenerate band around the X point. Inclusion of the SOC effect opens up a tiny gap at the anticrossing point of bands along the Γ-X direction. This is in accordance with the previous band-structure calculations on LaSb [22]. The corresponding Fermi-surface sheets of these bands, whose colors are in a one-to-one relationship, are given in Fig. 1(b). There are two hole pockets around the Γ point: The smaller one takes an isotropic spherical shape; the bigger one looks like three crossing spindles. The electron pockets are around the X points of the first BZ. When we move half of these pockets to the equivalent opposite X points, they will form three ellipsoids with the long principal axis pointing along the Γ-X direction. By computing the volumes of the electron and hole pockets, we obtain the hole-type and electron-type carrier densities as 2.10×10^{20} and 2.20×10^{20} cm^{-3} (Table I),

TABLE I. Electron-type (α band) and hole-type (β and γ bands) carrier densities (in units of 10^{20} cm^{-3}) and their ratios for LaSb and LaBi calculated with the PBE functional at the GGA level and the MBJ potential at the meta-GGA level, respectively.

	LaSb		LaBi	
	PBE	MBJ	PBE	MBJ
$n_e(\alpha)$	2.20	0.38	3.45	1.65
$n_h(\beta)$	0.43	0.08	0.71	0.31
$n_h(\gamma)$	1.67	0.32	2.95	1.31
N_e/N_h	1.05	0.95	0.94	1.02

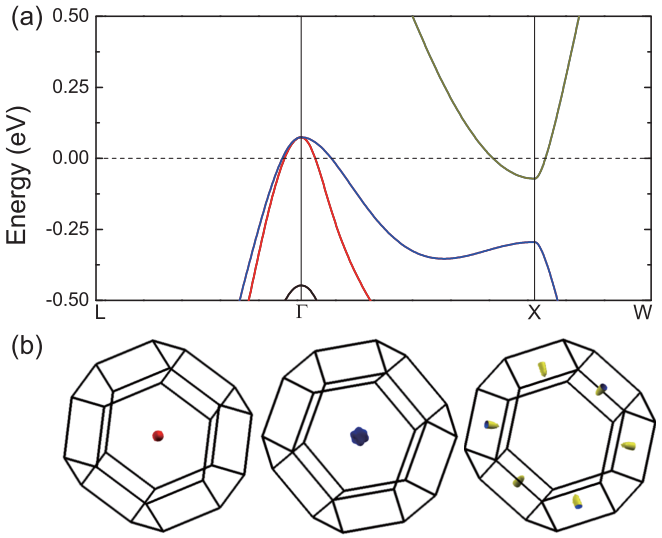

FIG. 2. (a) Band structure along high-symmetry directions of the Brillouin zone and (b) Fermi surface of LaSb calculated with the MBJ potential and including the SOC effect.

respectively. They are in the same order of magnitude as those measured in the transport experiment [13]. The ratio between the densities of electron-type carriers and hole-type carriers is 1.05, indicating a compensation between the electrons and the holes.

As LaSb is a semimetal, we have also studied its band structure and Fermi surface with the MBJ potential in the meta-GGA level. Compared with the band structure calculated with the PBE functional [Fig. 1(a)], the dramatic changes in Fig. 2(a) can be discerned. The tops of two doubly degenerate valence bands at the Γ point shift downwards about 0.2 eV, whereas the bottom of the doubly degenerate conduction band at the X point shifts upwards. These band shifts yield an obvious reduction of the Fermi-surface volumes [Fig. 2(b)] and thus lead to the decrease in carrier densities (Table I). Moreover, in the MBJ calculations, there is no anticrossing of bands along the Γ-X direction, which seems to lift the overlap between valence band and conduction band in the PBE calculations [Fig. 1(a)]. A similar phenomenon was also noticed by Tafti *et al.* [13]. More information on the bands below the Fermi level around the X point can be obtained from their orbital weights and corresponding charge densities as follows. On the other hand, although the carrier densities reduce sharply, the elaborate calculation using dense k points in the whole BZ renders the carrier-densities' ratio between electrons and holes as 0.95, which is in good accordance with the ratio $[0.014/(0.004 + 0.011) = 0.93]$ measured in the previous de Haas–van Alphen effect experiment [24,26]. Thus no matter whether the calculations are using the PBE functional at the GGA level or the MBJ potential at the meta-GGA level (Table I), the charge compensation in LaSb always holds.

To analyze the changes in band characteristics at the X point of the Brillouin zone (Figs. 1 and 2), we have plotted the band structures with orbital weights and the band decomposed charge densities calculated with the PBE functional in Fig. 3 and with the MBJ potential in Fig. 4, respectively. In the PBE

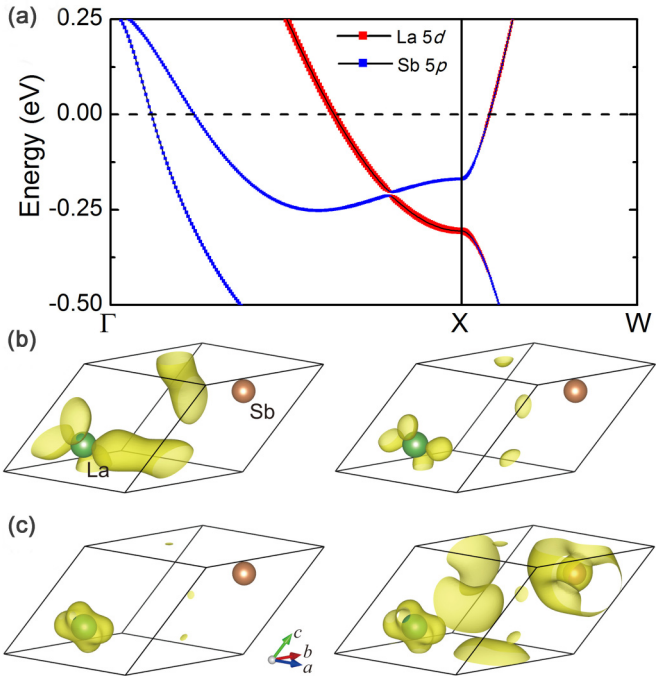

FIG. 3. (a) Band structure of LaSb with the orbital weights around the X point calculated with the PBE functional and including the SOC effect. Band decomposed charge densities of LaSb for two doubly degenerate bands with energies (b) −0.31 eV and (c) −0.17 eV below the Fermi level at the X point.

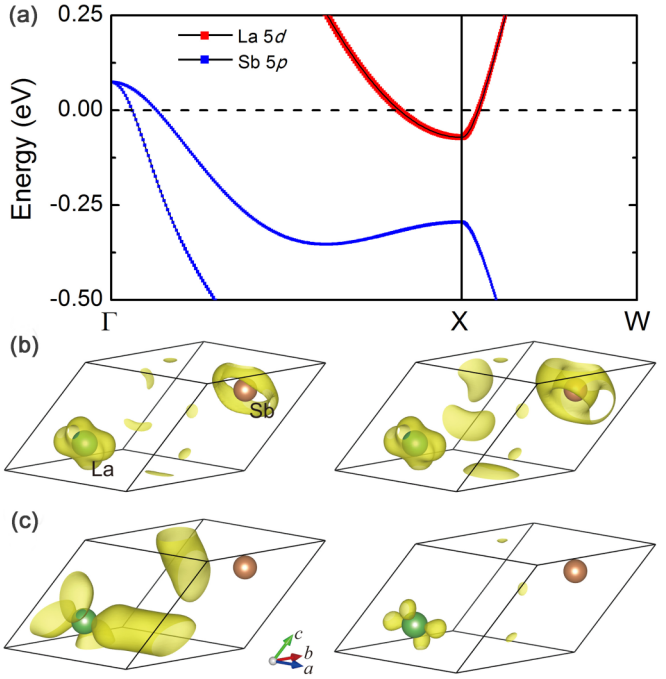

FIG. 4. (a) Band structure of LaSb with the orbital weights around the X point calculated with the MBJ potential and including the SOC effect. Band decomposed charge densities of LaSb for two doubly degenerate bands with energies (a) −0.29 eV and (b) −0.07 eV below the Fermi level at the X point.

calculation, for the two doubly degenerate bands along the Γ-X direction [Fig. 3(a)], a band inversion can be discerned from their orbital weights. Moreover, the charge densities for the bands with energy −0.31 eV below the Fermi level at the X point [Fig. 3(a)] mainly distribute around the La atom [Fig. 3(b)]. On the other hand, the bands with energy −0.17 eV below the Fermi level at the X point [Fig. 3(a)] also demonstrate some charge distributions around the Sb atom [Fig. 3(c)]. The higher-energy (−0.17-eV) conduction band with charges on the anion atom and the lower-energy (−0.31-eV) valence band with charges on the cation atom imply a band inversion at the X point as also revealed by Zeng *et al.* [22]. However, when the MBJ potential is adopted, the above band characteristics change thoroughly. From the orbital weights, there is no band inversion along the Γ-X direction [Fig. 4(a)]. For the two doubly degenerate bands with energies −0.29 and −0.07 eV at the X point [Fig. 4(a)], their corresponding charge densities are displayed in Figs. 4(b) and 4(c), respectively. The lower-energy (−0.29-eV) valence band with charges on the anion atom Sb [Fig. 4(b)] and the higher-energy (−0.07-eV) conduction band with charges on the cation atom La [Fig. 4(c)] indicate no band inversion at the X point. Thus, whether the calculations with the PBE functional or those with the MBJ potential offer the correct band structure of LaSb around the X point needs experimental verification, such as angle-resolved photoemission spectroscopy (ARPES) measurement.

B. LaBi

The band structure and Fermi surface of LaBi calculated with the PBE functional and including the SOC effect are shown in Fig. 5. In the element periodic table, Bi belongs to the same main group as Sb but with a heavier mass and a larger atomic radius. Compared with the 5p orbitals of Sb, the Bi 6p orbitals are more extended. This will induce more wave-function overlap with the La atom when forming the rock-salt structural crystal LaBi as reflected in

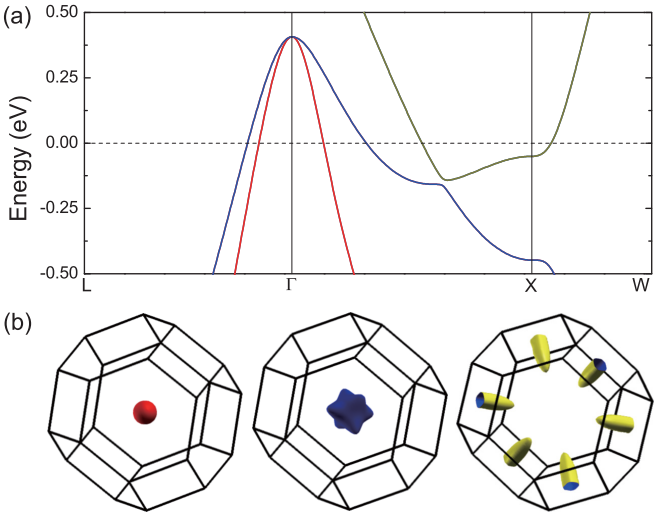

FIG. 5. (a) Band structure along high-symmetry directions of the Brillouin zone and (b) Fermi surface of LaBi calculated with the PBE functional and including the SOC effect.

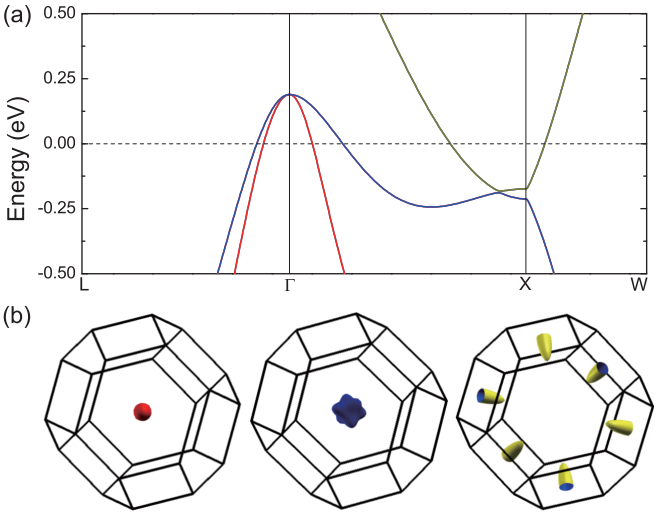

FIG. 6. (a) Band structure along high-symmetry directions of the Brillouin zone and (b) Fermi surface of LaBi calculated with the MBJ potential and including the SOC effect.

the higher energies of the valence-band top around the Γ point [Fig. 5(a)] and the larger overlap area between two anticrossing bands around the X point than that of LaSb [Fig. 1(a)]. In addition, due to the heavier mass of Bi than Sb, the SOC effect in LaBi is more prominent. As a result, the band gap along the Γ-X direction is more notable [Fig. 5(a)]. These features in the band structure of LaBi are consistent with those reported in the previous calculations using the GGA functional [22]. Meanwhile, the Fermi-surface volume of LaBi [Fig. 5(b)] is larger than that of LaSb [Fig. 1(b)], which leads to higher carrier densities ($\sim 3.5 \times 10^{20}$ cm^{-3}) for both electrons and holes (Table I). The calculated densities are on the same order of magnitude with the values estimated from magnetotransport measurements [20]. The ratio between the densities of electron-type and hole-type carriers is 0.94, revealing an electron-hole balance in LaBi as well [20].

Similar to LaSb, when the MBJ potential is applied in the calculations, the band structure and Fermi surface of LaBi also show some obvious changes (Fig. 6). Compared with the PBE results [Fig. 5(a)], downward shifting for the valence-band top at the Γ point and upward shifting for the conduction-band bottom at the X point are found. However, due to the larger overlap between the valence and the conduction bands in LaBi than that of LaSb, the introduction of the MBJ potential does not eliminate the overlap completely as indicated by the reserved band overlap below the Fermi level at the X point [Fig. 6(a)]. On the other hand, the band shifts cause the reduction of both Fermi-surface volume [Fig. 6(b)] and carrier densities (Table I). Nevertheless, the calculated density ratio between electron-type and hole-type carriers is 1.02 (Table I), i.e., in a charge compensation as well. This is in accordance with the measured ratio [$0.027/(0.0064 + 0.022) = 0.95$] in the previous de Haas–van Alphen effect experiment [24,26].

Since both the PBE functional and the MBJ potential calculations reserve the band overlap around the X point of the

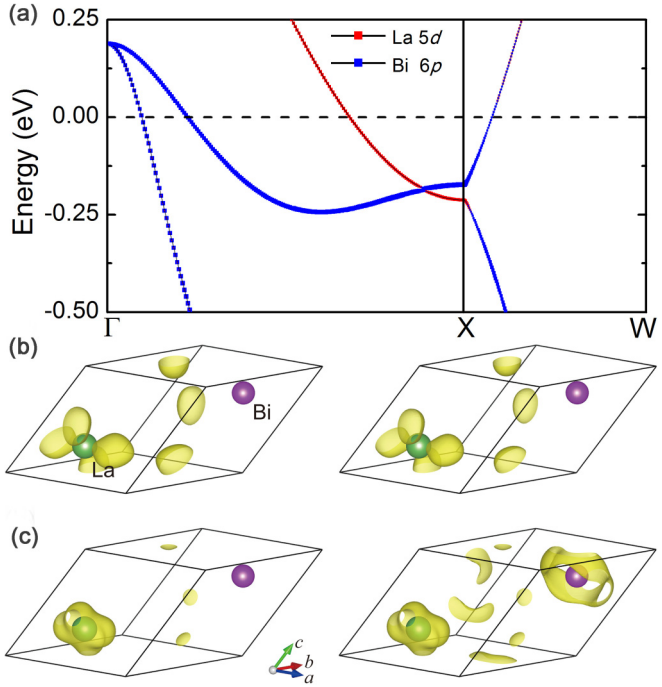

FIG. 7. (a) Band structure of LaBi with the orbital weights around the X point calculated the MBJ potential and including the SOC effect. Band decomposed charge densities of LaBi for two doubly degenerate bands with energies (a) −0.21 eV and (b) −0.17 eV below the Fermi level at the X point.

BZ for LaBi (Figs. 5 and 6), we plot in Fig. 7 the band structure with orbital weights and the band decomposed charge densities calculated with the MBJ potential for illustration. Near the X point, a band inversion can be perceived from the orbital weights [Fig. 7(a)]. Moreover, the lower-energy (−0.21-eV) band at the X point displays charge distributions around the cation atom La [Fig. 7(b)], whereas the higher-energy (−0.17-eV) band also shows some charge distributions around the anion atom Bi [Fig. 7(c)]. Thus for LaBi, a band inversion around the X point exists, which agrees with the findings by Zeng *et al.* [22] and Hasegawa [24]. In addition to the charge compensation (Table I), the topological effect in LaBi may introduce some interesting topological surface states on certain surfaces [22], which may interact with its XMR anisotropically.

IV. DISCUSSION

From the semiclassical two-band model, the electrical resistivity of nonmagnetic materials with both electron-type and hole-type carriers under a vertical magnetic field reads [42,43]

$$\rho(B) = \frac{(n_e\mu_e + n_h\mu_h) + (n_e\mu_h + n_h\mu_e)\mu_e\mu_h B^2}{e(n_e\mu_e + n_h\mu_h)^2 + e(\mu_e\mu_h)^2(n_e - n_h)^2 B^2}, \quad (1)$$

where n_e (n_h) is the electron (hole) concentration, μ_e (μ_h) is the mobility of electrons (holes), e is the charge unit of the electron, and B is the magnetic field. Then the magnetoresistance, which describes the change in electrical resistance in response to the magnetic field, yields

$$\mathrm{MR} = \frac{\rho(B) - \rho(0)}{\rho(0)} = \frac{n_e\mu_e n_h\mu_h(\mu_e + \mu_h)^2 B^2}{(n_e\mu_e + n_h\mu_h)^2 + (n_e - n_h)^2(\mu_e\mu_h)^2 B^2}. \quad (2)$$

When the charge compensation is satisfied ($n_e = n_h$), the MR shows a quadratic dependence on the magnetic field with the product of electron-type and hole-type carrier mobilities as the coefficient,

$$\mathrm{MR} = \mu_e\mu_h B^2. \quad (3)$$

We first concentrate on the magnetoresistances of LaSb and LaBi as well as their relationship with the magnetic field. Our above calculations have shown that the electron and hole carriers nearly fulfill the compensation (Table I), thus Eq. (3) can be applied. This naturally explains the quadratic dependence of MR on the magnetic field and its nonsaturating behavior observed in LaSb [13,19] and LaBi [19–21]. On the other hand, Eq. (3) indicates that the MR is proportional to the carrier mobility product. Since the mobility μ equals $e\tau/m^*$, the longer the mean-free time τ and the smaller the carrier effective mass m^*, the higher the mobility μ. Our calculated carrier densities of semimetals LaSb and LaBi are quite low (Table I), thus the carriers would have a long mean-free time and thus high mobility at low temperatures. In fact, the derived carrier mobilities of LaSb and LaBi from low-temperature transport experiments do manifest high values (10^4–10^5 cm^2 V^{-1} s^{-1}) [13,20,21] comparable to that found in WTe_2 [10,13]. From Eq. (3), these high carrier mobilities would result in extremely large MRs, which are observed in LaSb [13,19] and LaBi [19–21]. Our calculated results with charge compensation and low carrier densities (Table I) consistently interpret the XMR and its nonsaturating quadratic magnetic-field dependence found in LaSb and LaBi.

The temperature effect is prominent in the recently found nonmagnetic XMR materials, which all demonstrate metallic behavior at high temperatures and the turn on of MR at low temperatures [10–13]. The origin of the resistivity enhancement at low temperatures has been well addressed by Wang *et al.*: instead of a magnetic-field-induced metal-insulator transition, it is due to the opposite temperature dependences of the ordinary resistivity at zero magnetic field and the other part induced by the magnetic field [44]. Another interesting phenomenon found in lanthanum monopnictides is the resistivity plateau below ∼15 K [13,20]. Previously, the resistivity plateau in LaSb was compared with a similar plateau protected by the conducting surface states of a topological insulator candidate SmB_6 [13]. In fact, the resistivity plateau in LaSb can also be understood within the framework of a semiclassical two-band model as in LaBi [20]. Our calculations show that LaSb is in electron-hole balance $n_e = n_h = n$ (Table I), then from Eq. (1), the resistivity becomes

$$\rho(T,B) = \frac{1 + \mu_e(T)\mu_h(T)B^2}{en(T)[\mu_e(T) + \mu_h(T)]}. \quad (4)$$

The dependence of resistivity $\rho(T,B)$ on temperature T is included in the temperature-dependent carrier densities $n(T)$ and mobilities $\mu(T)$. At very low temperatures without thermal

excitation, the carrier densities are nearly constant. On the other hand, as mentioned above, the mobility equals $e\tau/m^*$. Below very low temperatures: The lattice parameters and band structure change little, then the effective mass m^* of the carriers will not show much variation; moreover, the crystal lattice is frozen, and the mean-free time τ depends on carrier scattering. The τ is inversely proportional to the carrier densities, which will approach a constant at very low temperatures. Actually, the derived carrier densities and mobilities of LaBi from transport measurements indeed access constants at very low temperatures [20]. As a result, from Eq. (4), the nearly constant n and μ will induce a resistivity plateau under very low temperatures, which is observed in LaSb [13].

The carrier densities in semimetals depend sensitively on the Fermi level. Due to the low carrier densities of LaSb and LaBi (Table I), a slight change in Fermi level would induce a large variation of the density ratio between different types of carriers. We take LaSb for example. Within the PBE functional calculations, a 10-meV (corresponding to a temperature of 116 K) downward shift of the Fermi level would change the ratio N_e/N_h from 1.05 to 0.79, whereas a 20-meV shift yields 0.71. With the MBJ potential, a 10-meV downward shift of the Fermi level would vary the ratio from 0.95 to 0.59 and a 20-meV shift to 0.33. This obvious change in charge compensation would have a substantial reflection in the MR. The susceptible carrier ratio in LaSb to the Fermi level draws our attention when interpreting the experimental findings since surface adsorption or surface vacancies after exfoliation can easily tune the potential for the surfacial layers of LaSb and LaBi. Instead, compared with the three-dimensional rock-salt structures of LaSb and LaBi, the layered structure of bulk WTe_2 with weak interlayer interaction makes its interior more inert to surface adsorption. In other words, the nonsaturating quadratic XMR of bulk WTe_2 is more robust to surface modification.

One may notice that until now, we have not resorted to the topological effect when elucidating the XMR found in LaSb and LaBi. In our calculations using the MBJ potential, LaSb does not show band inversion around the X point (Figs. 2 and 4) whereas LaBi does (Figs. 6 and 7), thus these two lanthanum monopnictides may own different topological properties. However, due to their charge compensation, low carrier densities (Table I), and high carrier mobilities [13,20,21], they both demonstrate nonsaturating quadratic XMR and resistivity plateaus at very low temperatures [13,20,21]. Since these magnetic-field and temperature-dependent behaviors can be well understood within the semiclassical two-band model, they should be the common features of electron-hole compensated semimetals, no matter whether the materials are topological or not.

V. CONCLUSION

By using the first-principles calculations, we have systematically studied the electronic structures of the recently discovered XMR semimetals LaSb and LaBi. Despite the two different levels of exchange-correlation energy adopted, namely, the PBE functional in the GGA level and the MBJ potential in the meta-GGA level, we draw the same conclusions: (i) both LaSb and LaBi are in electron-hole compensation and (ii) the carrier densities are on the order of 10^{20} cm^{-3} as semimetals. From the semiclassical two-band model, these features combined with the high carrier mobilities derived from transport experiments [13,20,21] naturally explain the nonsaturating quadratic XMR found in LaSb and LaBi as well as the resistivity plateau at very low temperatures. We also find that the charge compensation in the semimetals LaSb and LaBi depends sensitively on the Fermi-level position, thus one must be careful when interpreting related experimental data.

On the other hand, the PBE calculations on LaSb give inverse bands at the X point of the Brillouin zone whereas the MBJ calculations show no inversion. In comparison, due to a larger overlap between the valence and the conduction bands in LaBi, the usage of different types of exchange-correlation functional yields the same band inversion around the X point. Thus LaSb and LaBi may possess different topological properties. The correct band features of LaSb and LaBi around the X point need to be verified by experiments, such as ARPES measurement.

Our studies suggest that despite the topological properties, the nonsaturating quadratic XMR and the resistivity plateau at very low temperatures should be the universal behaviors of all semimetals in electron-hole balance for which these features can be captured by the semiclassical two-band model. Our first-principles calculations revealing the charge compensation in both LaSb and LaBi are very crucial to accurately understand their XMR phenomena found in experiments.

ACKNOWLEDGMENTS

We thank H.-C. Lei, S.-C. Wang, and T. Qian for helpful discussions. This work was supported by the National Natural Science Foundation of China (Grants No. 11190024 and No. 91421304). K.L. was supported by the Fundamental Research Funds for the Central Universities and the Research Funds of Renmin University of China (Grant No. 14XNLQ03). Computational resources have been provided by the Physical Laboratory of High Performance Computing at RUC. The Fermi surfaces were prepared with the XCRYSDEN program [45].

[1] W. Thomson, Proc. R. Soc. **8**, 546 (1857).
[2] J. M. Daughton, J. Magn. Magn. Mater. **192**, 334 (1999).
[3] C. Reig, M.-D. Cubells-Beltrán, and D. Ramírez Muñoz, Sensors **9**, 7919 (2009).
[4] J. Stöhr and H. C. Siegmann, *Magnetism: From Fundamentals to Nanoscale Dynamics* (Springer-Verlag, Berlin, 2006).
[5] A. B. Pippard, *Magnetoresistance in Metals* (Cambridge University Press, Cambridge, UK, 1989).
[6] M. N. Baibich, J. M. Broto, A. Fert, F. Nguyen Van Dau, F. Petroff, P. Eitenne, G. Creuzet, A. Friederich, and J. Chazelas, Phys. Rev. Lett. **61**, 2472 (1988).
[7] G. Binasch, P. Grünberg, F. Saurenbach, and W. Zinn, Phys. Rev. B **39**, 4828 (1989).

[8] M. B. Salamon and M. Jaime, Rev. Mod. Phys. **73**, 583 (2001).
[9] J. S. Moodera, L. R. Kinder, T. M. Wong, and R. Meservey, Phys. Rev. Lett. **74**, 3273 (1995).
[10] M. N. Ali, J. Xiong, S. Flynn, J. Tao, Q. D. Gibson, L. M. Schoop, T. Liang, N. Haldolaarachchige, M. Hirschberger, N. P. Ong, and R. J. Cava, Nature (London) **514**, 205 (2014).
[11] C. Shekhar, A. K. Nayak, Y. Sun, M. Schmidt, M. Nicklas, I. Leermakers, U. Zeitler, Y. Skourski, J. Wosnitza, Z.-K. Liu, Y.-L. Chen, W. Schnelle, H. Borrmann, Y. Grin, C. Felser, and B.-H. Yan, Nat. Phys. **11**, 645 (2015).
[12] T. Liang, Q. Gibson, M. N. Ali, M.-H. Liu, R. J. Cava, and N. P. Ong, Nat. Mater. **14**, 280 (2015).
[13] F. F. Tafti, Q. D. Gibson, S. K. Kushwaha, N. Haldolaarachchige, and R. J. Cava, Nat. Phys. **12**, 272 (2016).
[14] I. Pletikosić, M. N. Ali, A. V. Fedorov, R. J. Cava, and T. Valla, Phys. Rev. Lett. **113**, 216601 (2014).
[15] Y.-F. Zhao, H.-W. Liu, J.-Q. Yan, W. An, J. Liu, X. Zhang, H.-C. Wang, Y. Liu, H. Jiang, Q. Li, Y. Wang, X.-Z. Li, D. Mandrus, X. C. Xie, M.-H. Pan, and J. Wang, Phys. Rev. B **92**, 041104(R) (2015).
[16] A. A. Abrikosov, Phys. Rev. B **58**, 2788 (1998).
[17] R. Xu, A. Husmann, T. F. Rosenbaum, M.-L. Saboungi, J. E. Enderbya, and P. B. Littlewood, Nature (London) **390**, 57 (1997).
[18] J. Jiang, F. Tang, X.-C. Pan, H.-M. Liu, X.-H. Niu, Y.-X. Wang, D.-F. Xu, H.-F. Yang, B.-P. Xie, F.-Q. Song, P. Dudin, T. K. Kim, M. Hoesch, P. K. Das, I. Vobornik, X.- G Wan, and D.-L. Feng, Phys. Rev. Lett. **115**, 166601 (2015).
[19] F. F. Tafti, Q. Gibson, S. Kushwaha, J. W. Krizan, N. Haldolaarachchige, and R. J. Cava, Proc. Nat. Acad. Sci. USA doi:10.1073/pnas.1607319113.
[20] S.-S. Sun, Q. Wang, P.-J. Guo, K. Liu, and H.-C. Lei, arXiv:1601.04618.
[21] N. Kumar, C. Shekhar, S.-C. Wu, I. Leermakers, U. Zeitler, B.-H. Yan, and C. Felser, arXiv:1601.07494.
[22] M.-G. Zeng, C. Fang, G.-Q. Chang, Y.-A. Chen, T. Hsieh, A. Bansil, H. Lin, and L. Fu, arXiv:1504.03492.
[23] H. Y. Lv, W. J. Lu, D. F. Shao, Y. Liu, S. G. Tan, and Y. P. Sun, Europhys. Lett. **110**, 37004 (2015).
[24] A. Hasegawa, J. Phys. Soc. Jpn. **54**, 677 (1985).
[25] H. Kitazawa, T. Suzuki, M. Sera, I. Oguro, A. Yanase, A. Hasegawa, and T. Kasuya, J. Magn. Magn. Mater. **31-34**, 421 (1983).
[26] H. Kitazawa, Master's thesis, Tohoku University, 1982.
[27] J. P. Perdew, A. Ruzsinszky, J.-M. Tao, V. N. Staroverov, G. E. Scuseria, and G. I. Csonka, J. Chem. Phys. **123**, 062201 (2005).
[28] J. P. Perdew, J. A. Chevary, S. H. Vosko, K. A. Jackson, M. R. Pederson, D. J. Singh, and C. Fiolhais, Phys. Rev. B **46**, 6671 (1992).
[29] J. P. Perdew and M. Levy, Phys. Rev. Lett. **51**, 1884 (1983).
[30] L. J. Sham and M. Schlüter, Phys. Rev. Lett. **51**, 1888 (1983).
[31] A. D. Becke and E. R. Johnson, J. Chem. Phys. **124**, 221101 (2006).
[32] F. Tran and P. Blaha, Phys. Rev. Lett. **102**, 226401 (2009).
[33] P. E. Blöchl, Phys. Rev. B **50**, 17953 (1994).
[34] G. Kresse and D. Joubert, Phys. Rev. B **59**, 1758 (1999).
[35] G. Kresse and J. Hafner, Phys. Rev. B **47**, 558 (1993).
[36] G. Kresse and J. Furthmüller, Comput. Mater. Sci. **6**, 15 (1996).
[37] G. Kresse and J. Furthmüller, Phys. Rev. B **54**, 11169 (1996).
[38] J. P. Perdew, K. Burke, and M. Ernzerhof, Phys. Rev. Lett. **77**, 3865 (1996).
[39] J. M. Leger, D. Ravot, and J. Rossat-Mignod, J. Phys. C **17**, 4935 (1984).
[40] N. Marzari and D. Vanderbilt, Phys. Rev. B **56**, 12847 (1997).
[41] I. Souza, N. Marzari, and D. Vanderbilt, Phys. Rev. B **65**, 035109 (2001).
[42] N. W. Ashcroft and N. D. Mermin, *Solid State Physics* (Saunders College, New York, 1976).
[43] J. M. Ziman, *Electrons and Phonons* (Clarendon, Oxford, 1960).
[44] Y. L. Wang, L. R. Thoutam, Z. L. Xiao, J. Hu, S. Das, Z. Q. Mao, J. Wei, R. Divan, A. Luican-Mayer, G. W. Crabtree, and W. K. Kwok, Phys. Rev. B **92**, 180402(R) (2015).
[45] A. Kokalj, Comput. Mater. Sci. **28**, 155 (2003).